PCH PhysicoChemical Hydrodynamics Vol. 11, No. 5/6, pp. 625–644, 1989.
Printed in Great Britain

0191–9059/89 $3.00+.00
Pergamon Press plc

THERMOCAPILLARITY EFFECTS ON THE STABILITY OF BUOYANCY-DRIVEN FLOWS IN SHALLOW CAVITIES

H. BEN HADID, B. ROUX

IMFM, 1 rue Honnorat, 10003 Marseille, France

and

P. LAURE

Université de Nice, 06034 Nice Cedex, France

Abstract—The main objective of this paper is to show the influence of thermocapillary forces on the buoyancy-driven flow of low-Prandtl-number fluids in shallow cavities with differentially heated endwalls. The horizontal walls are considered as perfectly conducting with a linear temperature profile. The upper horizontal boundary is a free flat surface. Calculations were carried out by solving the Navier–Stokes equations and the computations concern large aspect ratio (length/height) $A = 25$ at fixed Prandtl number, $Pr = 0.015$. For two given Grashof numbers, 3×10^3 and 6×10^3, the Reynolds number was varied from negative to positive values. Such a combined convection problem is also investigated by means of stability theory. We look at the temporal stability of the analytical solution occurring in the core of a large cavity. It is found that critical Grashof number Gr_c for the onset of the oscillatory regime substantially decreases with small negative Re, and increases with positive Re. But, the thermocapillary forces have again an important stabilizing role for high negative values of Reynolds number (e.g. $Re < -400$, for $Pr = 0.02$). Direct numerical simulations exhibit a quite similar behaviour of the evolution of the critical Grashof number Gr_c, with respect to Re.

1. INTRODUCTION

Buoyancy- and thermocapillary-driven flows simultaneously occur in many systems with free surfaces relevant to a number of various fields. In reduced gravity environment, the buoyancy forces are reduced but still exist while the thermocapillary forces become dominant (Ostrach & Pradhan, 1978; Schwabe *et al.*, 1981). So, a flow results from combined action of buoyancy and thermocapillary forces. In the case of fluid convection in liquid metals under normal gravity (Hurle, 1974; Favier *et al.*, 1986), or in reduced-gravity environment (Schwabe & Scharmann, 1981a), it is now well known that an unsteady flow regime sets up as the thermal gradient is increased beyond some critical value. The majority of prior experimental works in this area were confined to transport liquid with high Prandtl number; relatively fewer works concerned liquid metals and can be found in survey papers of Pimputkar & Ostrach (1981), Azouni (1981) and Schwabe (1981b) and Roux *et al.* (1989b). This lack of experimental data such as velocity and temperature field in liquid metal is due to the specific difficulties in measuring such quantities in such kind of fluids (opacity, hot fluids, ...). Since many various industrial applications involve buoyancy and thermocapillary forces which strongly influence the flow regimes, it is of interest to investigate the flow resulting from their combined effect.

The general class of flows induced by thermocapillary force has been the subject of review articles by Levich & Krilov (1969), Kenning (1968) and Ostrach (1977). There are a number of analytical papers about thermocapillary flows in rectangular open cavities (see, for example the paper by Birikh (1966b). Smith & Davis (1983) and Davis (1987) performed

linear stability analysis of the thermocapillary-driven flows (subject to three-dimensional disturbances).

A number of experiments by Chun (1980) and Schwabe & Scharman (1984) in floating zones have shown complex behaviours (e.g. oscillations with amplitude modulation). By increasing the thermal gradients or the cavity height (Grashof number) different dynamical regimes of the flow were distinguished by examining the fluctuation values of the temperature at fixed location. Several investigators experimentally studied the problem of combined buoyant and thermocapillary flows in cavities (see for example works of Kamotani *et al.* (1982) in silicone oil and Fluorinert Fc-43, Schwabe & Scharmann (1981) in $NaNO_3$, Metzger & Schwabe (1988), Lamprecht *et al.* (1989), Villers & Platten (1985) in water–ethanol liquid, and Camel & Tison (1986) in liquid tin). Note that Camel & Tison (1986) experiments do not exhibit time-dependent flow, contrary to the Kamotani *et al.* (1982) experiments where temperature fluctuations were detected near the surface. These fluctuations have a relatively small magnitude and their behaviour is not as well defined as the one performed with the same liquid in float-zone configuration.

Numerical calculations of the thermocapillary-driven flows in open cavities were performed by Strani, Piva & Graziani (1983) for moderate aspect ratios ($A \leqslant 5$) and by Ben Hadid & Roux (1989b) for larger cavities ($A = 12.5$ and 25). Combined buoyant and thermocapillary flows in differentially heated cavity were studied by Zebib, Homsy & Meiburg (1985), Ben Hadid & Roux (1989c) and (1989d). Calculations for large aspect ratio $A > 4$, are not known to the authors.

The present study addresses the transition from laminar steady-state to oscillatory-state via two-dimensional direct numerical simulations and stability analysis. In order to study the resulting steady combined buoyant and thermocapillary flows, a number of calculations were made with values of Grashof number, $Gr = 3 \times 10^3$ and 6×10^3, below that of the first bifurcation in infinitely shallow cavity (after Hart (1983) and Laure & Roux (1987)). The Reynolds numbers were varied from negative (opposing effect) to positive values (adding effect). The results are presented for Prandtl number $Pr = 0.015$. This corresponds to liquid tin for which some experiments by Camel & Tison (1986) have already been reported by Ben Hadid *et al.* (1988).

2. PREVIOUS WORKS

It has been shown by means of stability analysis (Hart, 1972, 1983; Laure & Roux, 1987) that for infinitely long cavity with free surface, a first bifurcation to unsteady flow regime occurs at $Gr \approx 7890$ for $Pr \to 0$. Also, experimental works (Hurle, 1974; Hart, 1983) as well as numerical calculations for oscillatory buoyant flows (Winters, 1988; Ben Hadid & Roux, 1989a; and Pulicani *et al.*, 1990) show that the Gr_c increases with decreasing the length of the cavity (or the aspect ratio). So, for the present aspect ratio, $A = 25$, we expect that purely buoyancy-driven flow leads to a steady-state regime for Grashof numbers up to 6×10^3 (at least).

In a previous work, Ben Hadid & Roux (1989c) used hermitian finite-difference methods to emphasize the structure of oscillatory flow regimes. At $Pr = 0.015$, they noted the presence of a strong vortex in the cold region, for a moderate aspect ratio $A = 4$, and for $Gr < 5 \times 10^3$. When further increasing Gr, a stationary bifurcation is reached with the appearance of a secondary cell followed by a transition to unsteady flow. The first transition is a periodic flow which occurs, for $A = 4$ and $Pr = 0.015$, at $1.475 \times 10^4 < Gr < 1.5 \times 10^4$ and seems to persist with increasing Gr. The authors also noted that there is a reverse flow near the rigid bottom wall. This reverse flow exists in steady-state regime and becomes

pulsating (rising and filling) in unsteady regime. With increasing Gr, it expands to reach the upper boundary. The effect of the thermocapillary force on the established buoyant flow was emphasized considering the following ranges of Reynolds and Grashof numbers: $-2\times10^3 \leqslant Re \leqslant 8\times10^2$ and $1.45\times10^4 \leqslant Gr \leqslant 2\times10^4$. The main result is that small negative Re's (opposing effect) provide destabilizing forces. The frequency as well as the mean flow-rate decrease while, in contrast, the amplitude of the oscillations increases when Re decreases. On the contrary, for positive Re (adding effect), and starting from unsteady pure-buoyancy convection, we show that oscillations are damped and the flow reaches a steady-state as Re increases.

Winters (1986, 1987 and 1988) carried out two-dimensional (2D) calculations using bifurcation theory for purely buoyancy-driven flows in open cavities. He determined the critical Grashof number, Gr_c, for the transition from steady to unsteady flow. The results show that Gr_c decreases when the aspect ratio increases, and thus confirm, in a qualitative sense, the experimental results of Hurle (1974). The effect of the horizontal thermal boundary conditions was investigated numerically by Ben Hadid & Roux (1989) and Pulicani *et al.* (1990). The 2D results are in agreement with Winters' conclusions: Gr_c depends on the horizontal thermal boundary conditions (higher in the conducting case than in the insulating one).

In the experiments of Metzger & Schwabe (1988) and Lamprecht *et al.* (1989), combined buoyancy and thermocapillary effects were investigated for various Reynolds numbers, Grashof numbers and aspect ratios. In a square cavity and for low temperature differences (low Gr and Re), the authors observed that the fluid motions affect the whole cavity which is filled by one large vortex. As the temperature difference is increased the flow motions separate into two distinct parts each one with a complicated flow structure (thermocapillary-driven near the free surface and buoyancy-driven in the remaining part of the cavity). These qualitative experimental observations are more evident for $A = 0.5$ than for $A = 1$. Concerning the effects of buoyancy forces, the results of Metzger & Schwabe (1988) also show that the velocity near the surface is enhanced in both, opposing and adding, cases. So, the surface velocity is minimum for pure thermocapillary flow. The explanations of this feature were given by the authors; the buoyancy cell located below the surface tension cell plays a significant role in both cases. It propels the surface cell backflow in the oppposing case while in the adding case the hot liquid flowing up towards the hot corner under the action of buoyancy forces penetrates the surface cell and makes the thermal boundary layer thicker. Thus the accelerating thermocapillary force acts for a longer distance.

In previous work, Ben Hadid *et al.* (1988), experimental and numerical results for the surface velocity in shallow cavities show that there is a transition from viscous to boundary layer flow regime as the Reynolds number is increased. The limiting value of Re/A for the viscous regime was estimated to $Re/A < 20$ while the transition to the boundary layer regime occurs for $Re/A > 200$. For the boundary layer regime, the surface velocity in the middle of the cavity is given by a simple relationship which is:

$$v(x = 1, A/2) = 0.95(Re/A)^{-1/3} \quad \text{with reference velocity } v\ Re/H;$$

which shows a dependence of the surface velocity on the aspect ratio, and therefore on the length of the cavity. Furthermore, the experimental results of Metzger & Schwabe (1988) concerning the effects of the aspect ratio (their figure 25) for deep cavities show that in the pure thermocapillary flow case, no significant variation in the surface velocity was observed with lowering of the aspect ratio by increasing the height of the cavity. According to the above analysis, this result shows the difference on dynamical behaviours between deep and shallow cavities.

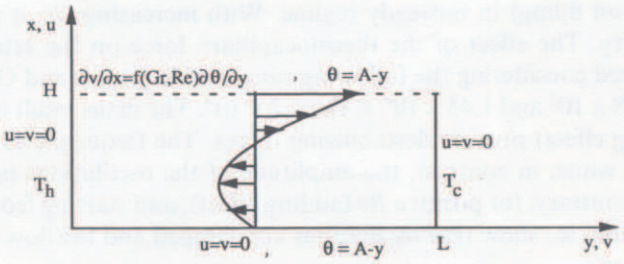

Fig. 1. Schematic representation of the two-dimensional model.

3. PROBLEM DESCRIPTION

We consider two-dimensional rectangular cavities of length L and height H filled with liquid metal (low Prandtl numbers). The vertical side walls of the cavities are maintained at different temperature T_h and T_c, where $T_h > T_c$ (Fig. 1). The horizontal boundaries are considered as perfectly conducting with a linear temperature profile. The upper boundary of the open cavity is assumed to be flat and subject to a surface tension, σ, which is related to temperature by a linear law: $\sigma = \sigma_0[1-\gamma(T-T_m)]$. The problem is non-dimensionalized by using ν/H^2, H, $\nu Gr/H$, and $\Delta T/A$, as reference quantities for time, length, velocity and temperature, respectively; where $\Delta T = T_h - T_c$ and ν is the kinematic viscosity.

When using the Boussinesq approximation, the governing equations in the vorticity-stream-function formulation are:

$$\frac{\partial \zeta}{\partial t} + Gr\left[u\frac{\partial \zeta}{\partial x} + v\frac{\partial \zeta}{\partial y}\right] = \frac{\partial^2 \zeta}{\partial x^2} + \frac{\partial^2 \zeta}{\partial y^2} + \frac{\partial \theta}{\partial y}; \tag{1}$$

$$\frac{\partial \psi}{\partial \tau} = \frac{\partial^2 \psi}{\partial x^2} + \frac{\partial^2 \psi}{\partial y^2} + \zeta; \tag{2}$$

$$\frac{\partial \theta}{\partial t} + Gr\left[u\frac{\partial \theta}{\partial x} + v\frac{\partial \theta}{\partial y}\right] = \frac{1}{Pr}\left[\frac{\partial^2 \theta}{\partial x^2} + \frac{\partial^2 \theta}{\partial y^2}\right]; \tag{3}$$

where ζ, ψ, and θ are the vorticity, the stream-function and the temperature, respectively, and τ is fictitious time introduced in equation (2), in order to accelerate the convergence procedure. The relevant independent dimensionless parameters are

$$A = L/H, \quad Pr = \nu/\kappa, \quad Gr = g\beta H^4 \Delta T/L\nu^2, \quad Re = (-\partial\sigma/\partial T)H^2\Delta T/L\rho\nu^2.$$

The above parameters represent the aspect ratio, the Prandtl number, the Grashof number, and the Reynolds number, respectively. In this paper the case $Pr = 0.015$ only is treated in the direct numerical simulations. For each Grashof number, the steady-state solutions for the largest Reynolds numbers were used for initial conditions. The relative magnitude of thermocapillary to buoyancy forces is given by the ratio $Re/Gr = (-\partial\sigma/\partial T)/\rho g\beta H^2$. We will also use, in the discussion of the results, the reciprocal of this ratio which is the dynamical Bond number, denoted Bo.

3.1. *Boundary conditions*

The problem involves two driving forces: the buoyancy force acting within the liquid in the whole cavity and the thermocapillary force which acts on the upper surface. The dynamical boundary condition on this upper surface connects the velocity gradient to the temperature gradient by the following dimensionless formula (see Birikh, 1966b):

$$\frac{\partial v}{\partial x} = \frac{Re}{Gr}\frac{\partial \theta}{\partial y}; \tag{4}$$

$$v(0,y) = u(0,y) = 0\,;\; u(1,y) = 0 \quad \text{and } \theta(0,y) = \theta(1,y) = A - y.$$

Since the upper surface is held at constant temperature gradient, surface tension gradients drive a constant surface-tension force and so the vorticity at the free surface remains constant.

4. STABILITY ANALYSIS

We look at linear stability of the 1D steady flow which exists for a long cavity ($A \to \infty$) in the y-direction (e.g. parallel to ∇T and perpendicular to g) as shown by Birikh (1966a, 1966b) for buoyancy and thermocapillary driven flows. Linear stability results have already been given by Hart (1983), Laure & Roux (1987), Kuo & Korpela (1988) for buoyancy convection. In the present paper, we study the influence of Marangoni effects on the appearance of the 2D oscillatory perturbations due to buoyant forces.

The governing system is given by the equations (1) to (3) (Navier–Stokes and energy), and the scaling factor for velocity is chosen as v/HGr. We also take perfectly conducting thermal conditions; the results will be essentially the same for adiabatic conditions (in fact the origin of these 2D perturbations are purely dynamical as shown by Roux *et al.* (1989a)).

The equations admit a particular 1D solution called Hadley circulation (see Hart (1972)). It gives $u = U_0(x)$ and $v = w = 0$. A vertical temperature profile $T_0(x)$ can be associated to $U_0(x)$, such that $\theta(x,y) = T_0(x) + y$. For Rigid–Free conducting horizontal boundaries the analytical expressions for $U_0(x)$ and $T_0(x)$ are given by the following:

$$U_0(x) = \frac{(8x^2 - 15x + 6)x}{48} - \frac{Re}{Gr}\frac{(3x-2)x}{4}; \tag{5}$$

$$T_0(x) = PrGr\left(\frac{x(x-1)(8x^3 - 17x^2 + 3x + 3)}{960} - \frac{Re}{Gr}\frac{x(x-1)(3x^2 - x - 1)}{48}\right). \tag{6}$$

The basic velocity U_0 is decomposed into two terms. The first one is due to buoyancy forces, the second one is the contribution of thermocapillary forces.

Let U, T and q denote the perturbations of the basic flow; they satisfy the following equations:

$$\begin{cases} \dfrac{\partial \vec{U}}{\partial t} + Gr[\vec{U}_0 \cdot \nabla \vec{U} + \vec{U} \cdot \nabla \vec{U}_0] + Gr[\vec{U} \cdot \nabla \vec{U}] = -\nabla\theta + \Delta \vec{U} + T\vec{e}_g, \\ \nabla \cdot \vec{U} = 0, \\ \dfrac{\partial T}{\partial t} + Gr[\vec{U}_0 \cdot \nabla T + \vec{U} \cdot \nabla T_0] + Gr[\vec{U} \cdot \nabla T] = \dfrac{1}{Pr}\Delta T, \end{cases} \tag{7}$$

with the boundary conditions

$$u = v = w = 0 \quad \text{for } x = 0,$$

$$\frac{\partial u}{\partial x} = \frac{\partial v}{\partial x} = 0\,; \quad w = 0 \quad \text{for } x = 1,$$

$$T = 0 \quad \text{for } x = 0 \quad \text{and } +1.$$

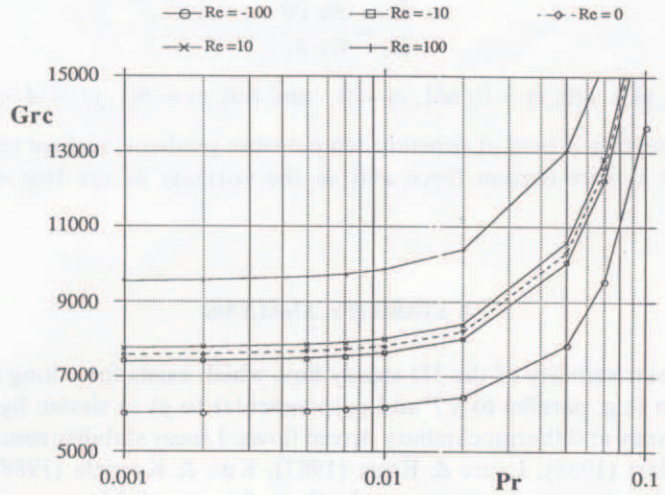

Fig. 2. The critical Grashof number Gr_c, with respect to Prandtl number Pr, for several Reynolds number $-100 \leqslant Re \leqslant 100$.

The linear stability is based on the Tau method (a variant of the Galerkin method where the boundary conditions are explicitly imposed). The perturbations are expressed with Fourier decomposition

$$Z = (U, T) = (\mathbf{U}(x), \mathbf{T}(x))e^{\lambda t}e^{i(hy+kz)}, \tag{8}$$

where the wavenumbers h and k are real, and λ is complex ($\lambda = \lambda_r + i\lambda_i$). In the following, the wavelengths $\lambda_y = 2\pi/h$ and $\lambda_z = 2\pi/k$, and the frequency $f = \lambda_i/2\pi$ are chosen with the scaling factors H and ν/H^2 repectively. Chebyshev expansions are employed in the x-direction: $U(x) = \Sigma T_n(x)$. As noted by Orszag (1971) and later by Brenier (1986), this Tau–Chebyshev method has been shown to be a very flexible and accurate technique. For a given Prandtl number, the critical Grashof number is calculated as $Gr_c = \inf_{h,k \in \Re} (Gr_0(h,k))$, where Gr_0 is the value of Gr such that the largest eigenvalues of the linearized perturbation equations are purely imaginary for given h and k. For the critical Gr_c this imaginary part may be zero (monotonic mode) or different from zero (oscillatory mode).

Without thermocapillary forces ($Re = 0$) the critical mode is 2D ($k = 0$) and oscillatory in the range $0 \leqslant Pr \leqslant 0.077$. For greater Prandtl numbers, 3D oscillatory mode ($k \neq 0$) becomes more unstable (see Roux *et al.* (1989b)). As shown in Fig. 2 (dashed line), the 2D-oscillatory branch asymptotically tends to a limit $Gr_c = 7590$, as Pr tends to 0, with a frequency close to 9. We also remark that for Re in the range -100 to 100, positive Reynolds numbers stabilize the basic flow, while negative Re favours the appearance of 2D oscillatory regime; the neutral curve moves up as we increase the Reynolds number.

However in the case of pure thermocapillary convection, the first bifurcation to unsteady regime for low-Pr is of 3D-nature (see Davis, 1983). Thus, we can also suppose that for high negative and positive Re the 2D-oscillation would disappear. Indeed, detailed computations made for $Pr = 0.001$, 0.005, 0.01 and 0.05 confirm that an important stabilization occurs for large $|Re|$. The evolution of the critical Grashof number and the critical frequency f with the Reynolds number Re are plotted in Figs 3 and 4, respectively. In Fig. 3, we note the existence of a minimum for negative Re, and, that the critical Grashof number Gr_c is connected with Re by a linear law ($Gr_c a_\pm Re + b_\pm$) for high positive and negative values of Re. This means that (i) Gr_c becomes infinite as $|Re| \to \infty$, (ii) the critical

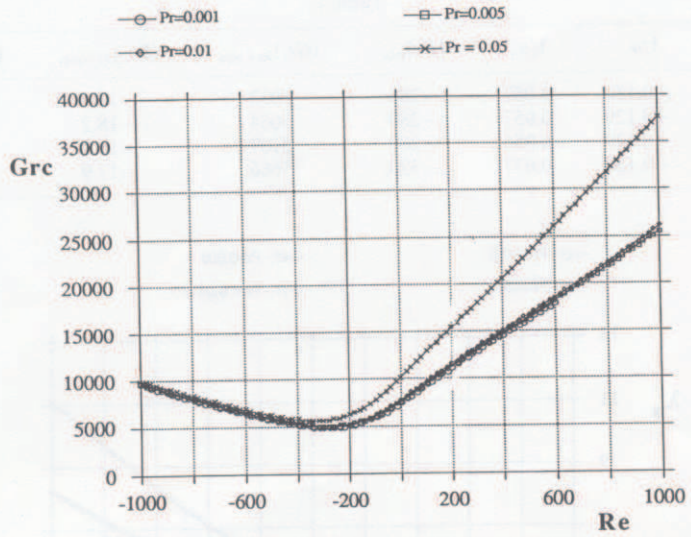

Fig. 3. Evolution of the critical Grashof number Gr_c, with respect to Reynolds number Re, for several Prandtl number $0.001 \leqslant Pr \leqslant 0.05$.

conditions for the onset of oscillation can be formulated in terms of dynamical Bond number ($Bo_c = a_+$ for $Re \gg 0$, and $Bo_c = a_-$ for $Re \ll 0$), and (iii) the flow does not become oscillatory if Re/Gr does not belong to the interval $[1/a_-, 1/a_+]$. From the former result, it is possible to derive some guide for specifying the experimental conditions for which such an oscillatory motion could occur:

$$\frac{1}{a_-} \leqslant -\frac{\dfrac{\partial \sigma}{\partial T}}{\rho g \beta H^2} \leqslant \frac{1}{a_+}. \tag{9}$$

But, let us note that the stability theory and this relation only apply if the two components

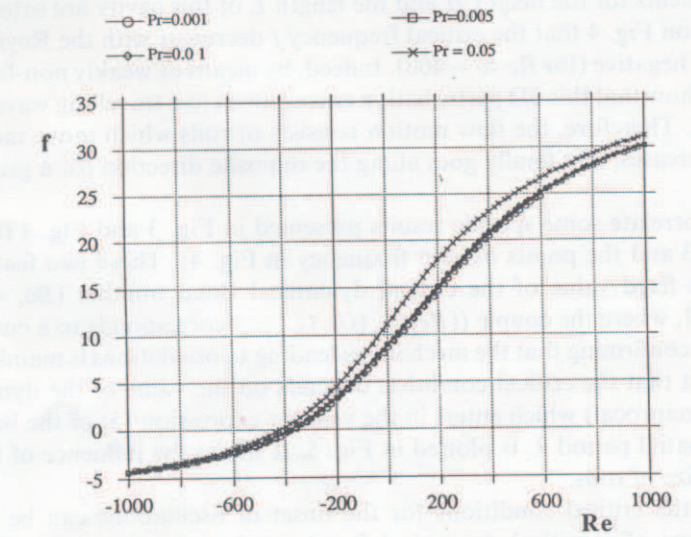

Fig. 4. Evolution of the frequency f, with respect to Reynolds number Re, for several Prandtl number, $0.001 \leqslant Pr \leqslant 0.05$.

Table 1

Pr	$1/a_-$	$1/a_+$	$(Re)_{\min}$	$(Gr_c)_{Re=\min}$	$(Bo_c)_{Re=\min}$	$(Bo_c)_{f=0}$
0.001	−0.130	0.057	−280	5033	−17.9	−13.7
0.005	−0.129	0.057	−280	5064	−18.2	−13.9
0.01	−0.129	0.056	−280	5107	−18.2	−13.9
0.05	−0.130	0.037	−320	5666	−17.9	−13.7

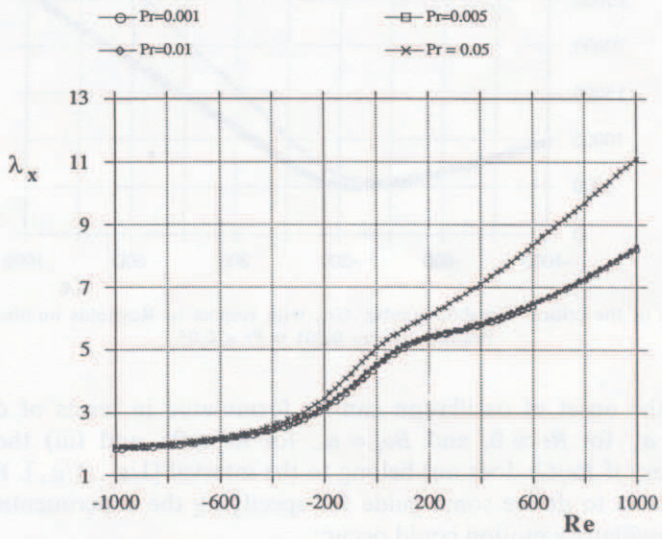

Fig. 5. Evolution of the critical spatial period λ_x, with respect to Reynolds number Re, for several Prandtl number $0.001 \leqslant Pr \leqslant 0.05$.

of the basic flow corresponding to buoyant and thermocapillary effects (see equation (5)) correspond to fully developed regimes. And we know that fully developed regimes (mainly the one for thermocapillary convection) can only be observed in the core of a finite cavity, if some requirements for the height H and the length L of this cavity are satisfied.

We also note on Fig. 4 that the critical frequency f decreases with the Reynolds number Re and becomes negative (for $Re \approx -400$). Indeed, by means of weakly non-linear analysis, it is possible to show that this 2D perturbation corresponds to a travelling wave propagating along the y-axis. Therefore, the flow motion consists of rolls which move more and more slowly as Re decreases, and finally goes along the opposite direction for a given (negative) value of Re.

We tried to correlate some specific results presented in Fig. 3 and Fig. 4 (e.g. the curve minima in Fig. 3 and the points of zero frequency in Fig. 4). These two features seem to correspond to a fixed value of the critical dynamical Bond number ($Bo_c = Gr_c/Re$), as shown in Table 1, where the couple $((Re)_{\min}, (Gr_c)_{Re=\min})$ corresponds to a curve minimum in Fig. 3. That is confirming that the mechanism leading to oscillations is mainly dynamical; and thus the fact that the critical condition depends on the value of the dynamical Bond number (or its reciprocal) which enters in the velocity expression (5) of the basic flow.

The critical spatial period λ_x is plotted in Fig. 5. It shows the influence of the Reynolds number on the size of rolls.

In summary, the critical conditions for the onset of oscillations can be conveniently expressed in terms of a critical dynamical Bond number, for a wide range of positive and negative Re. For positive Re, Bo_c is nearly constant, with $Bo_c \approx 17.5$ in the interval

$0 < Pr \leqslant 0.05$; but this constant is changed for higher Pr (e.g. $Bo_c \approx 27.5$ for $Pr = 0.05$) indicating the beginning of some thermal effect on the dynamical field. In the case of opposing effect ($Re < 0$), Bo_c varies in the range $-400 < Re < 0$, but in such a way that $(Bo_c)_{Re=\min}$ and $(Bo_c)_{f=0}$ are constant; while Bo_c is nearly constant in the ranges $0 < Pr \leqslant 0.05$ and $-10^3 \leqslant Re < -400$ (with $Bo_c \approx -7.6$).

5. NUMERICAL SIMULATION

5.1. *Numerical procedure*

We solved the governing equations (1)–(3) using an A.D.I. (Alternating Direction Implicit) technique with a finite-difference method involving forward differences for time derivatives and hermitian relationships for spatial derivatives (see Hirsh (1974), Roux *et al.* (1979)).

In order to accurately describe gradients in boundary layers at large Reynolds numbers it is necessary to use a non-uniform grid. The need for a non-uniform grid also arises since the flow is non-symmetric even at moderate Reynolds numbers, and strong vortices occur in the cold region and occupy nearly one third of the cavity for increasing Re. Thus, grid refinement is needed near the boundaries and in this "vortex region" in cold side. A coordinate transformation, as the one proposed by Thompson (1974), is used to refine the grid. The computations were performed with a number of grid points varying with the guessed flow regime. Thus, we used 21*201 non-uniform grid points to simulate steady non-symmetric flow and for some cases (mainly the unsteady flow regime) a 21*401 uniform grid points has been used. Simulations of two-dimensional buoyancy-driven convection have demonstrated the importance of an adequate resolution. For low-Prandtl fluids it is found that insufficient number of grid points in the boundary regions delayed the onset of the unsteady flow regime without affecting the overall pattern of the fluid flow. We have performed some resolution tests by increasing the number of grid points in each spatial direction. Further increasing the resolution (from 21*121 grid points to 31*161 grid points) only gave small differences (less than 5%) for steady flow regimes.

5.2. *Unsteady flow results*

As mentioned in a previous study (Ben Hadid & Roux (1989c)) and shown in the above section, there is a transition region in which the combined buoyant and thermocapillary flow changes from steady-state to oscillatory state. For a cavity with large aspect ratio $A = 25$, numerical calculations were done for a wide range of negative Re numbers ($Re > -1.67 \times 10^3$). Obviously the coupling is expected to be more intricate in the case where buoyancy and thermocapillary forces are opposing with the same intensity. For $Gr = 6 \times 10^3$ the steady-state regime appears to extend from $Re = 0$ to roughly $Re \approx -200$, where a transition to a time-dependent state occurs. A complex temporal behaviour, depending on the value of Grashof number, exists in some range of negative Reynolds numbers. In fact, for $Gr = 6 \times 10^3$ the flow regime which is steady at $Re = 0$ loses its stability for $-500 < Re < -200$. For this range of Reynolds numbers the unsteady flow regime prevails and for a slightly lower value ($Re \approx -500$) a strong restabilization is observed. While for $Gr = 3 \times 10^3$ a steady-state was found to prevail over all the investigated Reynolds number range. In fact, in some ranges of negative Re an unsteady multicellular flow regime sets up. Some information about the spatial structure of this oscillatory flow can be obtained by looking at the flow fields shown in Fig. 6(a–g) which correspond to seven (regularly spaced) times through the period. In this case the transient calculations have been carried out for

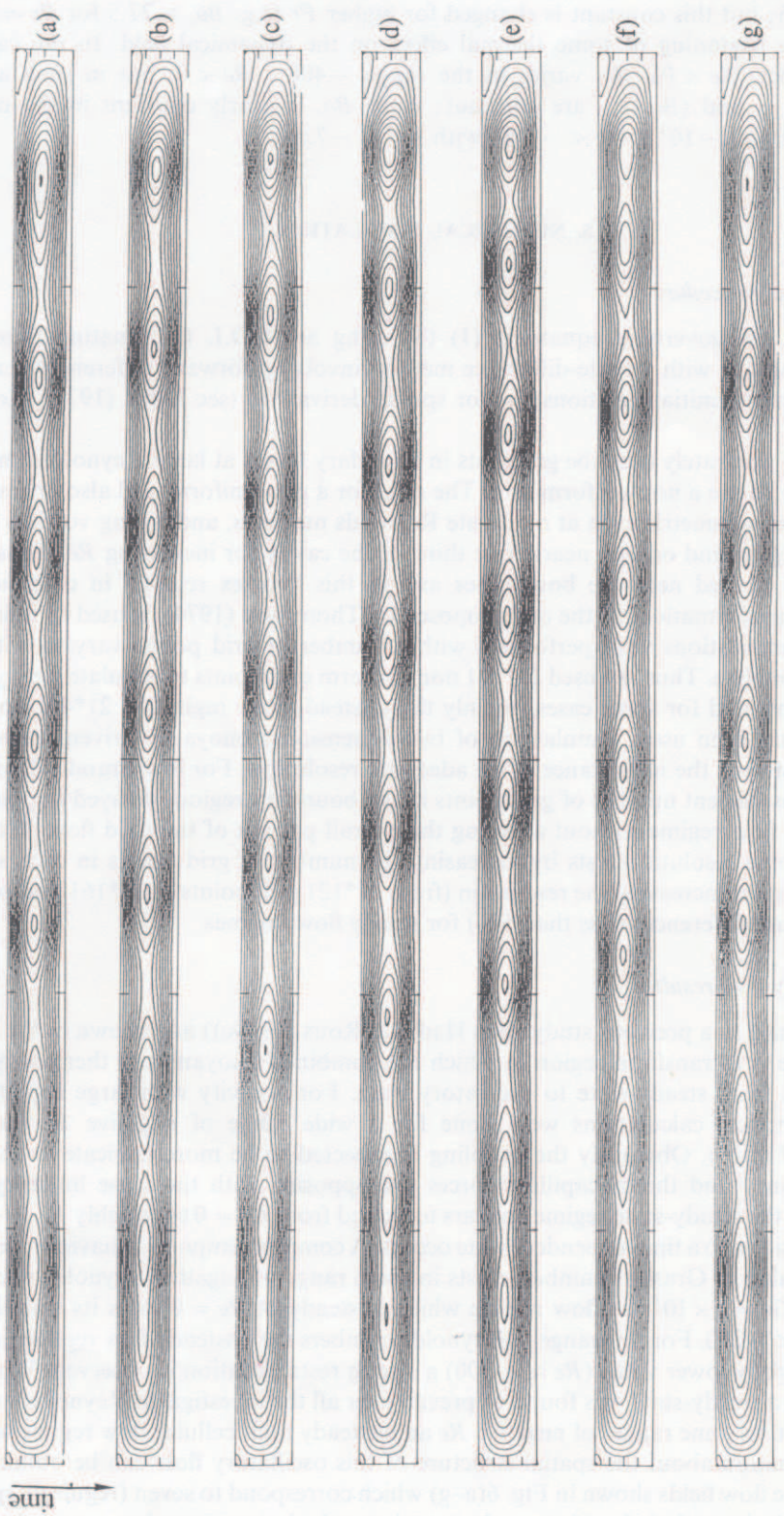

Fig. 6. Iso-ψ patterns (for $Gr = 6 \times 10^3$ and $Re = -300$) corresponding to seven (regularly spaced) time steps through a cycle of oscillation. Contour-lines are separated by equal intervals of $\delta\psi$ corresponding to 1/12 of the maximum in each frame.

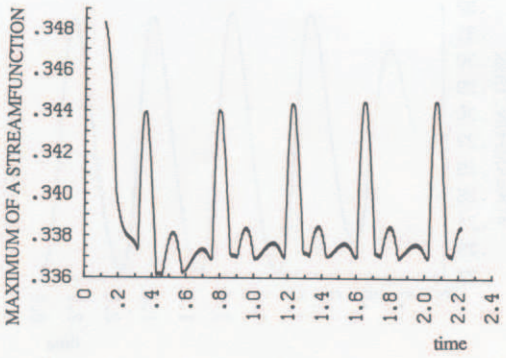

Fig. 7. Time-history of a maximum of a stream-function for $Gr = 6 \times 10^3$ and $Re = -300$.

a long enough time, in order to reach the regime of constant amplitude fluctuations. The time interval between each frame is $\Delta t = 3.6 \times 10^{-2}$ and represents 36 time steps. The ψ-contours are regularly spaced, but the $\Delta\psi$ interval has a different value in each frame. Each of Figs 6 exhibits a global circulation, along the horizontal walls, flowing from left to right (from hot to cold) at the top of the cavity, and in opposite sense at the bottom. It also presents several internal cells affecting the middle region (mid-height) of the cavity. Throughout a cycle, the number of these internal cells varies from seven (e.g. Figs 6a and 6g) to eight (Figs 6d and 6e). During such a cycle, the cells move from right to left; a new cell is created near the hot side (Fig. 6d), while in the cold region the cells are compressed and finally collapse (Figs 6f and 6g).

A typical time history of the maximum of the stream-function is displayed in Fig. 7 for $Re = -300$ and shows the initial transient behaviour leading to oscillations. The relative amplitude of the fluctuation of the maximum of the stream-function, $\Delta\psi_m = \Delta\psi_{\max}/\psi_{\max}$, is 6.14% for $Re = -200$ with a dimensionless frequency of $f = 4.32$. The fluctuation amplitude and frequency are found to decrease with a negative Reynolds number (i.e. $\Delta\psi_m = 2.4\%$ and $f \approx 2.38$ for $Re = -300$). Note that these quantities were found in previous works (see Roux (1989b)) to be very sensitive to the mesh resolution. The grid used is thought to be sufficient for the value of the parameters considered herein and it would prohibitively increase the computing time to further increase this grid. Furthermore, the time evolution of the stream-function through the cavity shows that the fluctuation amplitude continuously increases from left to right. This variation of the amplitude of fluctuations is roughly estimated to 30%. The time-history of the stream-function at $x = 0.5$ is plotted for two horizontal locations corresponding to $y = 0.25 \times A$ in Fig. 8 and $y = 0.75 \times A$ in Fig. 9; these curves give additional information regarding the unsteady flow which oscillates with a single frequency.

5.3. *Steady flow results*

The streamline patterns are given in Figs 10 and 11 for the two Grashof numbers (3×10^3 and 6×10^3), and for several positive Reynolds numbers (with $0 \leqslant Re \leqslant 10^4$). In all these figures the flow is steady and circulates from left to right (from hot to cold) at the upper surface. A vortex already appears near the cold wall for $Re = 0$ (Fig. 10a), the strength of which increases with Re. Additional corotative cells are created as Reynolds number is increased (e.g. Figs 10d–10k). Thus, the flow is strongly asymmetric. As already mentioned for the case of pure thermocapillary-driven flow (Ben Hadid & Roux (1988)), the loss of

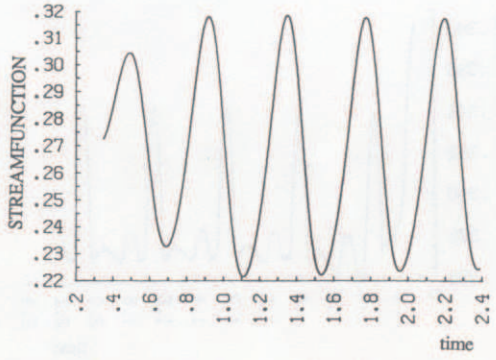

Fig. 8. Time-history of a stream-function (for $Gr = 6 \times 10^3$ and $Re = -300$) at $x = 0.5$ and $y = 0.25 \times A$.

flow symmetry is due to the loss of symmetry in the boundary conditions (the bottom is rigid while the upper free surface is subject to a shear force acting in one given direction).

For the two Grashof numbers and at a given Reynolds number, the flow appears qualitatively, to have a similar structure: a multicellular region which develops in front of the cold wall and a boundary layer region occupying the remaining part of the cavity. These two regions become more evident for high Reynolds numbers, where numerous corotative cells exist. Essentially the number of cells is higher for $Gr = 6 \times 10^3$ than for $Gr = 3 \times 10^3$. Moreover, as the Reynolds number increases, a small counter-rotating flow appears at the bottom wall between the primary cells (in the cold side), whereas in the remaining region of the cavity, the surface and backflow form a layer which becomes thinner with increasing *Re*'s. Furthermore, near the free surface the streamlines are more crowded indicating that the highest velocity is there, while a large zone with relatively small velocity exists at the bottom.

To focus attention on the case of opposing thermocapillary- and buoyancy-forces, computations were carried out for $Gr = 3 \times 10^3$ and for Re/Gr ranging from zero to -5.5 (i.e. $\infty \leqslant Bo < -0.18$). For this large range of investigated negative Reynolds numbers, two separated flows exist (see Figs 12); one is generated by buoyancy forces, rising along the hot wall (left side) and circulating from cold to hot along the upper surface. These two flows have nearly the same strength for $Bo \approx -6$ (Fig. 12d), giving rise to two superimposed cells occupying all the length of the cavity. The results presented in Figs 12e–l for large enough $|Re|$, where thermocapillarity dominates (i.e. $Bo > -6$), can be compared to the

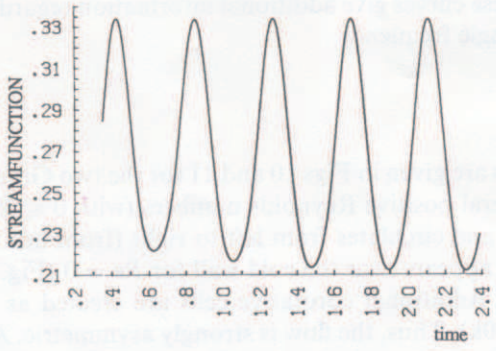

Fig. 9. Time-history of a stream-function (for $Gr = 6 \times 10^3$ and $Re = -300$) at $x = 0.5$ and $y = 0.75 \times A$.

Fig. 10. Streamline patterns for $Gr = 3 \times 10^3$ and several positive Reynolds numbers: (a) 0, (b) 333, (c) 667, (d) 10^3, (e) 1.333×10^3, (f) 2×10^3, (g) 2.667×10^3, (h) 3.333×10^3, (i) 5×10^3, (j) 6.667×10^3, (k) 10^4.

Fig. 11. Streamline patterns for $Gr = 6 \times 10^3$ and several positive Reynolds numbers: (a) 67, (b) 333, (c) 667, (d) 10^3, (e) 1.333×10^3, (f) 2×10^3, (g) 2.667×10^3, (h) 3.333×10^3, (i) 5×10^3, (j) 6.667×10^3, (i) 10^4.

Fig. 12. Streamline patterns for $Gr = 3 \times 10^3$ and several negative Reynolds numbers: (a) -67, (b) -167, (c) -333, (d) -500, (e) -667, (f) -10^3, (g) -1.333×10^3, (h) -2×10^3, (i) -3.333×10^3, (j) -5×10^3, (k) -6.667×10^3, (l) -10^4.

case of positive Re; they correspond to a flow circulating in the opposite direction (from cold to hot along the upper surface); but the main flow structure is qualitatively the same (except a very small recirculating buoyancy-driven flow in the bottom right corner).

The experiments of Villers & Platten (1987) in rectangular cavity filled with water-*n*-heptanol mixture show that the two kinds of convection exist in some range of the cavity height. Two separated counter-rotating cells occupy the cavity with the upper one thermocapillary-driven and the lower one buoyancy-driven. Below a certain value of the cavity height the buoyancy-driven cell vanishes to finally disappear. This behaviour is, also, well consistent with the streamline patterns in Fig. 12.

It is interesting to note that when increasing the positive Reynolds number, the present calculations never showed any flow separation to occur. This remark is supported by the calculations of Bergman & Keller (1988), for $Pr = 0.01$ and for lower aspect ratio $A = 0.5$, 1 and 2. Under these conditions, the flow induced by the combined driving forces was investigated for several values of the dynamic Bond number and exhibited, qualitatively, the same flow structure in the two cases of purely buoyancy-driven flow and combined adding effect. In the former case, an increase in the strength of the flow recirculation is evident from the values of the stream-function in the center of the cells. For positive Bo, the flow in a square cavity ($A = 1$) forms one great cell occupying all the volume, while for negative Bo (opposing effect), two cells separated by a tilted interface develop. For a cavity with an aspect ratio $A = 2$ and for $Bo_{\text{Bergman}} = BoA^2 = -10$, the calculations of Bergman & Keller (1988) show two cells, each one occupying nearly one half of the cavity with an extension of the thermocapillary cell up to the surface. For a higher $|Bo|$ (e.g. $Bo_{\text{Bergman}} = -100$) the flow structure changes; thermocapillary flow manifests itself on thin layer close to the upper surface while the buoyant flow dominates over the cavity. Furthermore, Bergman & Ramadhyani (1986) calculations for opposing driving forces ($Bo_{\text{Bergman}} = -10$) and for $Pr = 5$, show two superposed cells separated by a horizontal interface, and having nearly the same strength. Thus, this observed discrepancy in the flow structure, suggests the likelihood of owing to the effect of Pr number. Note that the study of Zebib *et al.* (1986) shows a strong change in the flow structure when the Prandtl number is varied from $Pr = 0.01$ to 50. The center of the strong vortex and subsequently the maximum of surface velocity, are located in front of the cold wall for low Prandtl numbers, and in front of the hot wall for $Pr = 50$. Despite the fact that this result is for purely thermocapillary-driven flow, it gives insight on the interaction of the fluid flows and thermal fields for intermediate values of Pr.

In Fig. 13, we give the plot of the surface velocity at the middle of the cavity for three Grashof numbers, $Gr = 3 \times 10^3$, $Gr = 6 \times 10^3$ and $Gr = 0$ which represent the pure thermocapillary flow. From this figure, it is clear that as Reynolds increases, the influence of buoyancy effects diminishes and the surface velocity will eventually coincide with the predicted values for $Gr = 0$ at high Re number. The thermocapillary flow is nearly independent of the varied Grashof number and, thus, is always the dominating factor for higher Reynolds numbers. The influence of the buoyancy force is limited at low Reynolds values, there is no appreciable variation on the surface velocity with Grashof number for Re higher than about 3×10^3. The experimental results of Metzeger & Schwabe (1988) concerning the effects of the aspect ratio (their figure 25) show that for shallow cavity ($A = 2$) the buoyancy force appears to have a little influence on the surface velocity in comparison to that for the pure thermocapillary flow. In fact, from their figure 25, the plot of the surface velocity for different aspect ratios, and therefore for different Grashof numbers (as the variation of the aspect ratio in the experiments, is due to the variation of the height of the cavity), the influence of the increasing Grashof number has more effect for deep cavities than for shallow cavities.

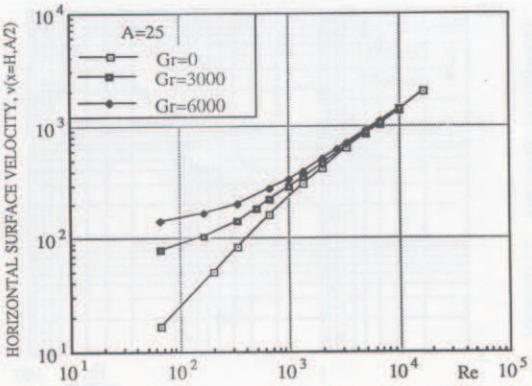

Fig. 13. Surface velocity at the middle of the cavity as a function of positive Reynolds numbers and for three Grashof numbers: $Gr = 0$, 3×10^3 and 6×10^3.

In the case of opposite buoyancy and thermocapillarity ($Re < 0$), the flow fields are drastically different, it is therefore interesting to see how the behaviour of the surface velocity may be changed. The inversion of the main flow is clearly shown in Fig. 14. In this figure we observe that the value of the surface velocity at higher $|Re|$ remains dependent on Gr unlike the case $Re > 0$. A correlation of the data has been attempted with the form:

$$\log (v_{\text{surf}}) = c \log [|Re|/Gr^{3/4}]. \tag{10}$$

A logarithmic plotting of v_{surf} in terms of $|Re|/Gr^{3/4}$ is presented in Fig. 15; it exhibits a behaviour with a 2/3 power, for values of $|Re|/Gr^{3/4}$ exceeding nearly 2, in the ranges of $3 \times 10^3 \leqslant Gr \leqslant 6 \times 10^3$ and $4 \times 10^2 \leqslant |Re| \leqslant 10^4$. This allows us to derive the following approximate law:

$$v_{\text{surf}} = a + b|Re|^{2/3}/Gr^{1/2}. \tag{11}$$

Thus, for opposing buoyancy and thermocapillary forces and for large aspect ratio, $A = 25$, a transition to a boundary layer flow regime occurs for $Re/Gr^{3/4} > 2$. According to the expression (11), the dimensionless surface velocities (at $y = A/2$) in Fig. 14, are re-plotted with respect to $Re/Gr^{3/4}$ in Fig. 16. Our numerical results for opposing effect and for large

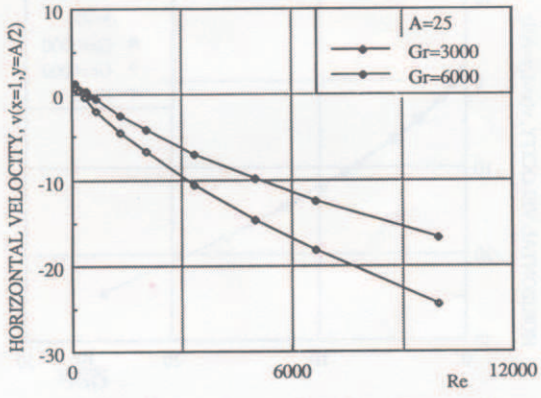

Fig. 14. Surface velocity at the middle of the cavity as a function of negative Reynolds numbers and for two Grashof numbers, $Gr = 3 \times 10^3$ and 6×10^3.

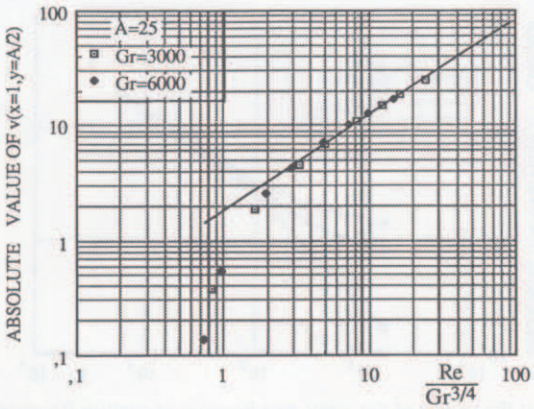

Fig. 15. Logarithmic plotting of the surface velocity at the middle of the cavity against $|Re|/Gr^{3/4}$.

cavity are seen to be very close to the plot of equation (11). The values of a and b entering in expression (11) can easily be derived from the correlation of the data which have been obtained for the two Grashof numbers $Gr = 3 \times 10^3$ and $Gr = 6 \times 10^3$. They are expected to depend on the dimensionless parameters, such as the aspect ratio. Indeed, a simple relationship has already been shown to exist in a previous paper by Ben Hadid *et al.* (1988) for the pure thermocapillary-driven flow, for which $a = 0$, and b is a function of A. In the present case ($A = 25$), the suggested values of the constant are the following: $a = 2.22$ and $b = -3.15$.

6. CONCLUSION

We have demonstrated by numerical simulation that a variety of flow structures and dynamical behaviours can occur in two-dimensional combined buoyant and thermocapillary convection when the aspect ratio is equal to 25. The effect of thermocapillary forces on the structure and the flow regime of the established buoyant flow has been

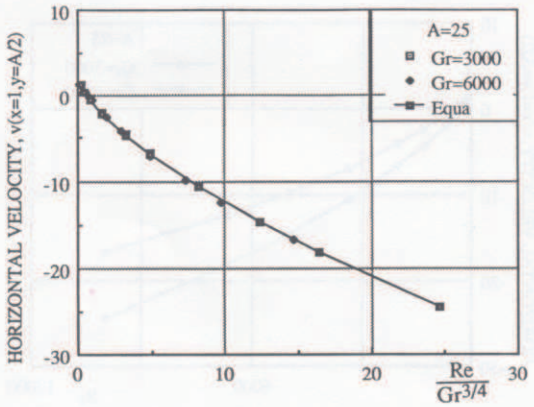

Fig. 16. Correlation of the surface velocity as a function of $|Re|/Gr^{3/4}$ for two Grashof numbers $Gr = 3 \times 10^3$ and 6×10^3.

emphasized both for adding ($Re > 0$) and opposing ($Re < 0$) cases. For $Re > 0$, a steady state flow regime prevails for all the investigated Re range and the surface velocity progressively becomes thermocapillary-controlled. As Re increases, several cells successively appear in the cold region where the highest velocity is located. The maximum number of cells depends on Gr and Re.

For negative Reynolds number (opposing effect), the most important result is that an unsteady flow regime set on for $Gr = 6 \times 10^3$, in some range of negative Reynolds numbers. The flow which would be steady for pure buoyancy, changes from steady to unsteady multicellular flow, and returns to steady multicellular flow when increasing $|Re|$. We did not completely explain all these results, but the onset of oscillation undoubtedly is of dynamical nature; the basic flow seems to become the most unstable for a specific value of the Bond number, $(Bo_c)_{Re=\min} \approx -18$, which is independent of the Prandtl number in the range $0 < Pr \leqslant 0.05$. We can conclude that the onset of oscillatory regime has certainly to be correlated to some property of the velocity profile $\mathbf{U}_0$ (e.g. the displacement of the inflexion point of this basic velocity $\mathbf{U}_0$), like in Tollmien–Schlichting stability results for forced convection, where the role of such an inflexion point in the velocity profile has been proved for the boundary layer stability. Note that such an inflexion point (which corresponds to the point where the second derivative of $\mathbf{U}_0$ vanishes, has to occur in the interval $0 \leqslant x \leqslant 1$; this is only possible, for the velocity profile (5), in the range $-0.416 \leqslant Re/Gr \leqslant 0.25$. In such a range the 2D-oscillatory regime can be found.

For smaller Gr (e.g. $Gr = 3 \times 10^3$), a steady-state solution prevails. When thermocapillary and buoyancy forces oppose each other ($Re < 0$), two separated flows exist; one is generated by buoyancy forces, rising along the hot wall (left side) and circulating from cold to hot along the bottom wall, while the second is thermocapillary-driven, circulating from cold to hot along the upper surface. These two flows have nearly the same strength for $Bo \approx -6$, giving rise to two superimposed cells occupying all the length of the cavity.

More experimental work would be done in order to give insight on the flow regimes (velocity fields and flow structures). We are currently working on the effect of aspect ratio and boundary conditions using numerical simulations.

Acknowledgements—This work was supported by the Centre National d'Etudes Spatiales (Division Microgravité Fondamentale et Appliquée), the Direction des Recherches Etudes et Techniques (Groupe 6), and the Centre de Calcul Vectoriel pour la Recherche. The authors also wish to thank J. J. Favier, D. Camel and P. Tison (L.E.S. of C.E.N.G.) for enlightening discussions.

REFERENCES

Ben Hadid, H. & Roux, B. (1989a) In, *Notes on Numerical Fluid Mechanics* (ed. B. Roux). Vieweg, Braunschweig.

Ben Hadid, H. & Roux. B. (1989b) Thermocapillary convection in long horizontal layers of low-Prandtl-number melts subject to horizontal temperature gradient. *J. Fluid Mech.* (In Press).

Ben Hadid, H., Roux, B., Laure, P., Tison, P., Camel, D. & Favier, J. J. (1988) Surface tension-driven flows in horizontal liquid–metal layers. *Adv. Space Res.* **8,** 265.

Ben Hadid, H. & Roux, B. (1989c) Buoyancy- and thermocapillary-driven flow in shallow open cavity: unsteady flow regimes, *J. Crystal Growth* **97,** 217–225.

Ben Hadid, H. & Roux, B. (1989d) Buoyancy and thermocapillary-driven flows in shallow cavities. (In press) ESA-SP.

Bergman, T. L. & Ramadhyani S. (1986) Combined buoyancy- and thermocapillary-driven convection in open square cavities. *Num. Heat Transfer* **9,** 441–451.

Bergman, T. L. & Keller, J. R. (1988) Combined buoyancy surface-tension flow in liquid metals. *Num. Heat Transfer* **13,** 49–63.

Birikh, R. V. (1966a) *J. Appl. Math. Mech.* **30,** 356–361.

Birikh, R. V. (1966b) Thermocapillary convection in horizontal layer of liquid. *J. Appl. Mech. Tech. Phys.* **7,** 43.

Brenier, B., Roux, B. & Bontoux, P. (1986) Comparaison des méthodes Tau–Chebyshev et Galerkin dans l'étude de stabilité des mouvements convection naturelle. *J. Mécanique Théor. Appl.* **5,** 95.

Camel, D., Tison, P. & Favier, J. J. (1986) Marangoni flow regimes in liquid metals. *Acta Astronautica* **13,** 723–726.
Chun, Ch. H. (1980) Experiments on steady and oscillatory temperature distribution in a floating zone due to the Marangoni convection. *Acta Astronautica* **7,** 479–488.
Davis, S. H. (1987) Thermocapillary instabilities. *Ann. Rev. Fluid Mech.* **19,** 403–435.
Favier, J. J., Rouzaud, A. & Comera, J. (1986) Influence of various hydrodynamic regimes in melts on solidification interface. *Rev. phys. Appl.* **22,** 195–200.
Hart, J. E. (1972) Stability of thin non-rotating Hadley circulations. *J. Atmos. Sci.* **29,** 687–697.
Hart, J. E. (1983) A note on the stability of low-Prandtl-number Hadley circulation. *J. Fluid Mech.* **132,** 271.
Hurle, D. T. J. (1967) Thermo-hydrodynamic oscillation in liquid metals: the cause of impurities striations in melt-grown crystals. *J. Phys. Chem. Solid*, Supplement No. 1, 659.
Hurle, D. T. J., Jakeman, E. & Jhonson, C. P. (1974) Convective temperature oscillations in molten gallium. *J. Fluid Mech.* **64,** 565–576.
Kamotani, Y., Ostrach, S. & Lowry, S. (1982) *Materials processing in the reduced gravity environment of space* (ed. Guy E. Rindone), pp. 161–171.
Kuo, H. P. & Korpela, S. A. (1988) Stability and finite amplitude natural convection in shallow cavity with insulated top and bottom and heated from a side. *Phys. Fluids* **31,** 33.
Laure, P. & Roux, B. (1987), Syntèse des résultats obtenus par l'étude de stabilité des mouvements de convection dans une cavité horizontale de grande extension. C.R.A.S., serie II, Tome 305, 1137–1143.
Metzger, J. & Schwabe, D. (1988) Coupled buoyant and thermocapillary convection. *PhysicoChem. Hydrodyn.* **10,** 263–282.
Orszag, S. A. (1971) Accurate solution of Orr–Sommerfeld stability equation. *J. Fluid Mech.* **50,** 166–208.
Ostrach, S. & Pradan, A. (1978) Surface-tension induced convection at reduced gravity. *AIAA J.* **16,** 419–424.
Pimputkar, S. M. & Ostrach, S. (1981) Convective effects in crystal grown from melts, *J. Crystal Growth* **55,** 614–646.
Pulicani, J. P., Crespo, E., Randriamampianina, A., Bontoux, P. & Peyret, R. (1990) *Int. J. Num. Meth. Fluids* (In press).
Roux, B., Ben Hadid, H. & Laure, P. (1989a) Numerical simulation of oscillatory convection in semiconductor melts. *J. Crystal Growth* **97,** 201–216.
Roux, B., Ben Hadid, H. & Laure, P. (1989b) Hydrodynamical regimes in metallic melts subject to a horizontal temperature gradient. *European J. Mech. B* **8,** 375–396.
Schwabe, D. (1981) Marangoni effects in crystal growth melts. *PhysicoChem. Hydrodyn.* **4,** 263–280.
Schwabe, D. & Scharmann, A. (1981) The magnitude of thermocapillary convection in large melt volumes, *Adv. Space Res.* **1,** 13–16.
Schwabe, D. & Scharmann, A. (1984) Measurements of the critical Marangoni number of the laminar-oscillatory transition of thermocapillary convection in floating zones. ESA SP-222.
Strani, M., Piva, R. & Graziani, G. (1983) Thermocapillary convection in rectangular cavity: asymptotic theory and numerical simulation. *J. Fluid Mech.* **130,** 347–376.
Smith, M. K. & Davis, S. H. (1983) Instabilities of dynamic thermocapillary liquid layers. Part 1. Convective instabilities. *J. Fluid Mech.* **132,** 119–144.
Winters, K. H. (1986) The onset of convection in a bounded fluid with a free surface. Harwell Report HL86/1335.
Winters, K. H., Clif, K. A. & Jackson, C. P. (1987) The prediction of instabilities using bifurcation theory. Harwell Report HL86/1147. In, *Transient and Coupled System*. John Wiley.
Winters, K. H. (1988) Oscillatory convection in liquid metals in a horizontal temperature gradient. *Int. J. Num. Meth. Engng* **25,** 401–414.